Research Article Vol. 32, No. 19 / 9 Sep 2024 / Optics Express 33159
Optics EXPRESS

Bound state in the continuum enabled ultralong silicon ridge waveguide grating antennas for integrated LiDAR applications

ZHIPENG MA,[1,2] YAO FU,[1,2] YUANJIAN WAN,[1,2] HAN CAO,[1,2] YU ZHANG,[1,2,*] AND JIAN WANG[1,2]

[1] *Wuhan National Laboratory for Optoelectronics, Huazhong University of Science and Technology, Wuhan 430074, Hubei, China*
[2] *Optics Valley Laboratory, Wuhan 430074, Hubei, China*
[*] *yuzhang87@hust.edu.cn*

Abstract: As a novel method for solid-state light detection and ranging (LiDAR), optical phased arrays (OPAs) cater to the growing market requirement for mass-produced chip-scale beam steering devices. Waveguide grating antennas (WGAs) with low loss, high efficiency and large emitting aperture are strongly desirable to achieve low beam divergence and high resolution for OPAs. In this paper, we report two kinds of silicon ridge-waveguide-based WGAs with ultra-sharp instantaneous field-of-view (IFOV) for LiDAR applications. The ridge-concave WGA (RCC-WGA) and ridge-convex WGA (RCV-WGA) are designed on account of both sides of ridge area have relatively weak mode field distribution. Lateral quasi-bound state in the continuum (L-BIC) is utilized to further suppress side scattering and improve the emission efficiency. The RCC-WGAs and RCV-WGAs are fabricated on silicon-on-insulator (SOI) platform with 220 nm device layer and foundry compatible etching depths. The measured losses are as low as 2.64 and 2.40 dB/mm at 1550 nm wavelength. The antenna length can up to 6 mm, with theoretical beam divergences of 0.0195° and 0.0175° at the wavelength of 1550 nm, while the experimental results are 0.0251° and 0.0237°, respectively. The proposed low-beam-divergence WGAs are promising in high resolution solid-state LiDAR applications.

1. Introduction

In recent years, automatic driving and unmanned aerial vehicle (UAV) have garnered a great deal of commercialization interest. LiDAR devices are key sensors for advanced driver assistance systems (ADAS). OPAs are able to realize solid-state beam steering pattern [1,2], which are widely used in LiDAR [3], free space optical (FSO) communication [4,5], imaging [6] and so on. The earlier OPAs are achieved at silicon platform or liquid crystal. OPAs are now moving towards to multi-material systems, higher integration, feature-rich, and better performance. Some other material platforms show great potential in solid-state LiDAR, like SiN [7,8], SiN-Si [9,10], thin film lithium niobate on insulator (LNOI) [11], InP [12,13] and so on. Silicon nitride is capable to load high power and avoids two-photon absorption (TPA) effect. LNOI platform has the unique advantages in high electro-optic modulation efficiency and low energy consumption, while III-V platform is more suitable to integrate light source. Moreover, hybrid integration [14,15] and 3D integration [16] are also potential schemes to combine the advantages of different materials on a wafer in the future.

Waveguide grating antennas are key components to achieve azimuthal-axis beam steering in OPAs. A large effective aperture would provide a high-resolution spot. In order to achieve millimeter length, multiple methods have been proposed including ultra-shallow etching [17], evanescent field modulation [18,19], multilayer structure [20,21] and chirped grating [22,23]. Most of these methods require modification from the standard fabrication process provided by

#534752 https://doi.org/10.1364/OE.534752
Journal © 2024 Received 3 Jul 2024; revised 16 Aug 2024; accepted 19 Aug 2024; published 29 Aug 2024

Optics EXPRESS

foundry services which are cost or requires complex process flow. As is known to all, ridge waveguide is not only a key passive waveguide structure but also widely used in silicon active devices, which effectively suppresses the sidewall scattering loss in strip waveguide.

Bound states in the continuum are superb conditions with infinite lifetime and infinite Q-factor [24]. Interference-based BICs exhibit remarkable potential in integrated optics like ultra-high-Q resonators [25–27], photonic integrated circuits (PICs) [28,29], nonlinear optics [30,31], gratings [32,33] and so on. Representative interference-based BICs mainly focus on leakage loss suppression for quasi-TM mode by adjusting the ridge width, as quasi-TM mode to TE slab mode transition happens in ridge waveguide. That is the quasi-TM mode located in the continuum of TE slab mode but still maintain bound state.

In this work, we demonstrate two kinds of 6mm-long WGAs with typical foundry provided etching depth, which are ridge-concave WGA (RCC-WGA) and ridge-convex WGA (RCV-WGA), respectively. This design principle lies in both sides of ridge area have relative weak mode field distribution, thus leads to ultra-low loss. Meanwhile, shallow-etched grating teeth gives rise upward perturbation to the mode field, which enables to accomplish a relatively high directivity of proposed WGAs in vertical direction. Lateral quasi-bound state in the continuum (L-BIC) is utilized to suppress side scattering. The proposed WGAs can achieve 6 mm emitting length, with the theoretical beam divergences of 0.0195° and 0.0175°, while the experimental results are 0.0251° and 0.0237°, respectively. The two WGAs behave high emission performance in the wavelength range of 1480-1580 nm, with the steering sensitivities of 13.43°/100 nm and 13.41°/100 nm. The measured steering ranges upon wavelength tuning are 1.28°/10 nm and 1.34°/10 nm. An imaging system is established to capture near-field and far-field patterns of WGAs. This work is an extension of our previous conference publication [34]. We provide further principle analysis and more comprehensive data on the device performance. The demonstrated WGAs are promising for high-resolution OPAs.

2. Design and simulation

The 3D perspective views of RCC-WGA and RCV-WGA are shown in Fig. 1. The two WGAs are designed at 220nm-SOI platform with 70 nm shallow etching to form the ridge and full etching to form the slab. The RCC-WGA is formed by partly inward etching to ridge waveguide, while the RCV-WGA is formed by ridge partly outward extension, which leads to a weak grating perturbation strength. The ridge width is marked as w_1, with the period of Λ. The Λ is set as 0.62μm to achieve a near vertical diffraction angle. To obtain low-loss WGA structures and suitable critical dimensions simultaneously, the grating teeth sizes are defined as (w2, a) = (70, 70) nm. In order to reduce the loss caused by the overlay misalignment, we set the slab width to be twice of the ridge width. This design also 'pushes' more electric field into slab area, thus has the benefit for restraining the waveguide side-wall scattering loss.

The mode profile of a 70nm-shallow etched ridge waveguide is shown in Fig. 2. The ridge width is 0.5μm, and slab width is double. It's evident that the mode profile is weak near ridge area, which preliminarily verify the rationality of our design method. By the way, though the both ends of slab region have weaker electric field distribution, we prefer to introduce upward perturbation to the mode field, so we still choose the shallow etched ridge waveguide grating structure. The wider slab is mainly used to provide overlay redundancy in fabrication.

The propagating mode in WGA is a disturbed mode rather than guided mode. Subject to periodic perturbation by grating teeth, the original TE guide mode excites different kinds of light fields, which are diffractive fields in vertical direction, lateral outward scattering fields and inner self-established fields. The various light fields distributions of two kinds of WGAs are shown in Fig. 3. Besides shallow-etched upward perturbation to the mode field, we also pursue higher upward diffractive field through lateral destructive interference between side scattering fields and self-established fields.

Optics EXPRESS

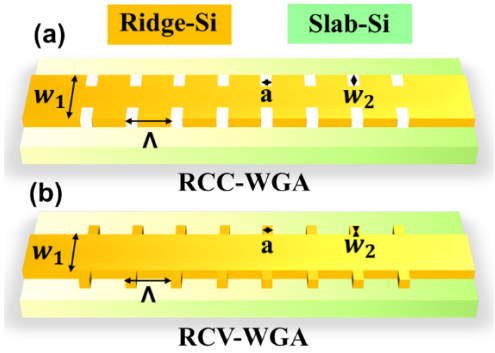

Fig. 1. 3D perspective schematics of (a) RCC-WGA and (b) RCV-WGA with some key parameters labeled. The two WGAs are designed based on 220nm-SOI platform with 70 nm shallow etched (With 2μm thick oxide on the top but not drawn).

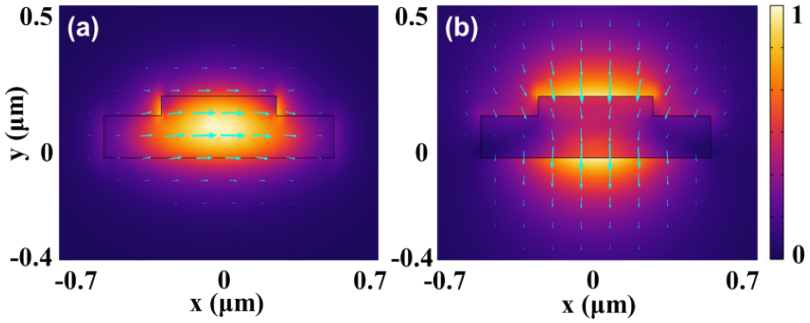

Fig. 2. The normalized modal field distributions of (a) TE_0 mode and (b) TM_0 mode in ridge waveguide with the ridge width of 0.5μm and slab width is double. The effective indexes of TE_0 mode and TM_0 mode are 2.660 and 1.825 at the wavelength of 1550 nm. The whole device height is 220 nm with the slab height of 150 nm. The outlines highlight the waveguide shape. Cyan arrows represent the directions of the electric field.

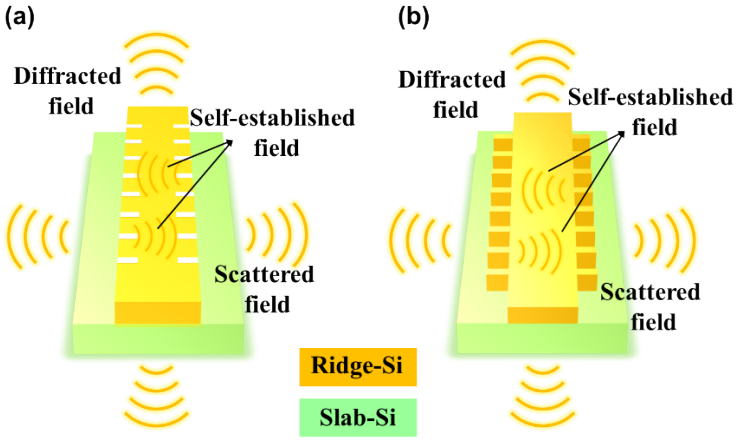

Fig. 3. 3D schematics of field distributions in (a) RCC-WGA and (b) RCV-WGA. The grating structures stimulate diffractive fields in vertical directions, side scattering fields and self-established fields in lateral direction. The L-BICs conditions are built via destructive interferences by scattering fields and self-established fields.

Optics EXPRESS

In our WGAs, the continuum state refers to the high-loss radiation mode while the bound state is low-loss disturbed quasi-TE_0 mode with minimum side scattering strength. The coupling strength κ of gratings can be expressed in Eq. (1) [21], $n_{eff,\lambda}$ is the average mode effective index in gratings, and $\Delta n_{eff,\lambda}$ is the difference value of mode effective index with or without gratings. By introducing the L-BIC, the coupling strength for RCC-WGA can be adapted as Eq. (2). and for RCV-WGA is adapted as Eq. (3) [32]. S_λ is the side scattering ratio and V_λ is the minimum vertical diffractive ratio. $n_{S,\lambda}$ is the effective index of scattering field or self-established field. Due to the stimulation of periodic perturbations, side scattering fields and self-established fields have initial phase difference, we mark it as $\varphi_{0,\lambda}$. When the ridge width changes, different degrees of destructive interference happened.

$$\kappa_\lambda = \frac{\Delta n_{eff,\lambda}}{n_{eff,\lambda} \times \Lambda} \tag{1}$$

$$\kappa_\lambda = \frac{\Delta n_{eff,\lambda}}{n_{eff,\lambda} \times \Lambda} \times \left| \frac{1 + (S_\lambda + V_\lambda)}{2} + \frac{1 - (S_\lambda + V_\lambda)}{2} \times exp\left\{ i \left[\frac{2\pi n_{S,\lambda}(w_1 - 2w_2)}{\lambda} + \varphi_{0,\lambda} \right] \right\} \right| \tag{2}$$

$$\kappa'_\lambda = \frac{\Delta n'_{eff,\lambda}}{n'_{eff,\lambda} \times \Lambda} \times \left| \frac{1 + (S'_\lambda + V'_\lambda)}{2} + \frac{1 - (S'_\lambda + V'_\lambda)}{2} \times exp\left\{ i \left[\frac{2\pi n'_{S,\lambda}(w_1)}{\lambda} + \varphi'_{0,\lambda} \right] \right\} \right| \tag{3}$$

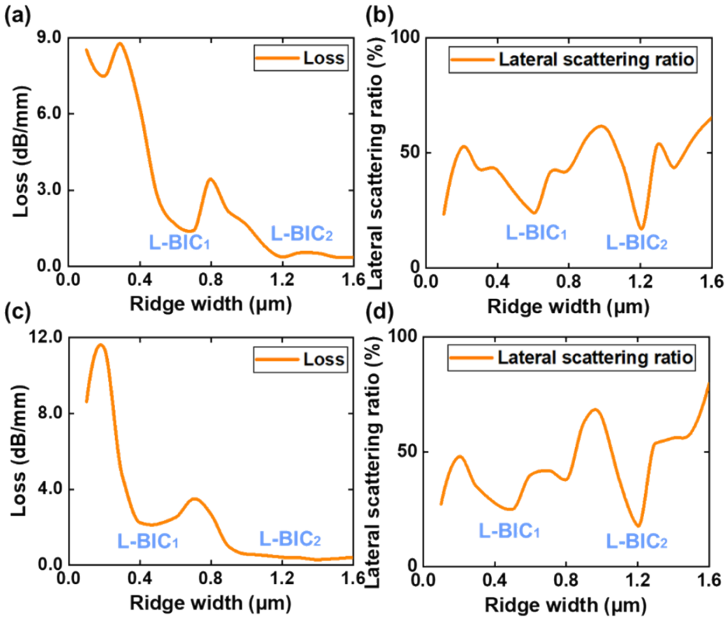

Fig. 4. Simulated (a) loss and (b) lateral scattering ratio for RCC-WGA. The 1-order L-BIC condition happen at the ridge width of 0.6μm while the 2-order L-BIC condition happen at that of 1.2μm. Simulated (c) loss and (d) lateral scattering ratio for RCV-WGA. The 1-order L-BIC condition happen at the ridge width of 0.5μm while the 2-order L-BIC condition happen at 1.2μm.

Optics EXPRESS

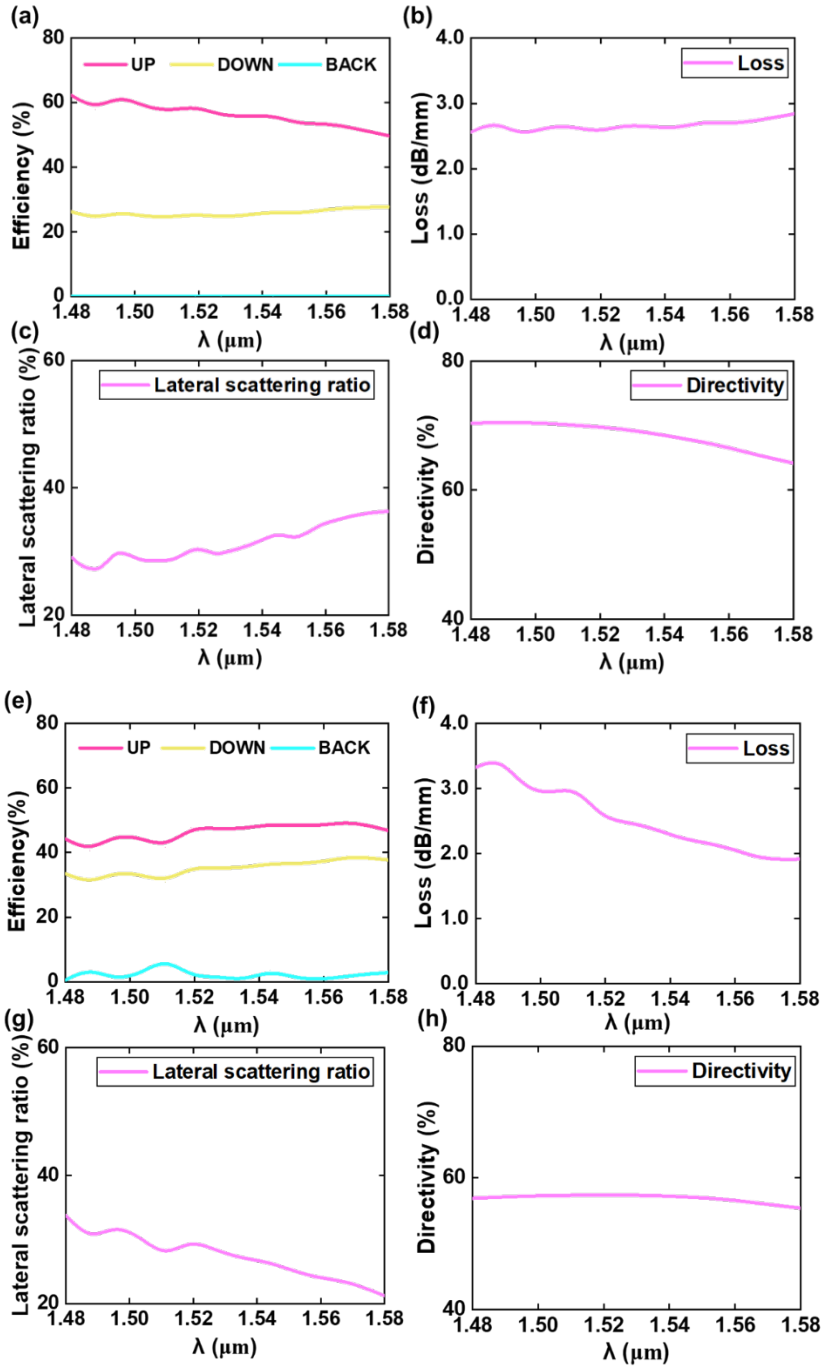

Fig. 5. The broad-spectrum performance of RCC-WGA from 1480-1580nm wavelength range. (a) Emitting efficiency in different directions. (b) Loss. (c) Lateral scattering ratio. (d) Directivity. And the broad-spectrum performance of RCV-WGA from 1480-1580nm wavelength range. (e) Emitting efficiency in different directions. (f) Loss. (g) Lateral scattering ratio. (h) Directivity.

Optics EXPRESS

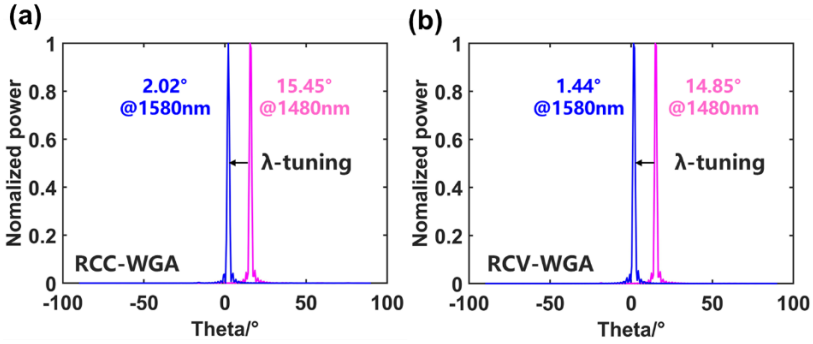

Fig. 6. The diffraction angles of (a) RCC-WGA and (b) RCV-WGA via the wavelength tuning from 1480 nm to 1580 nm. The steering angle of two WGAs are 13.43°/100 nm and 13.41°/100 nm, respectively.

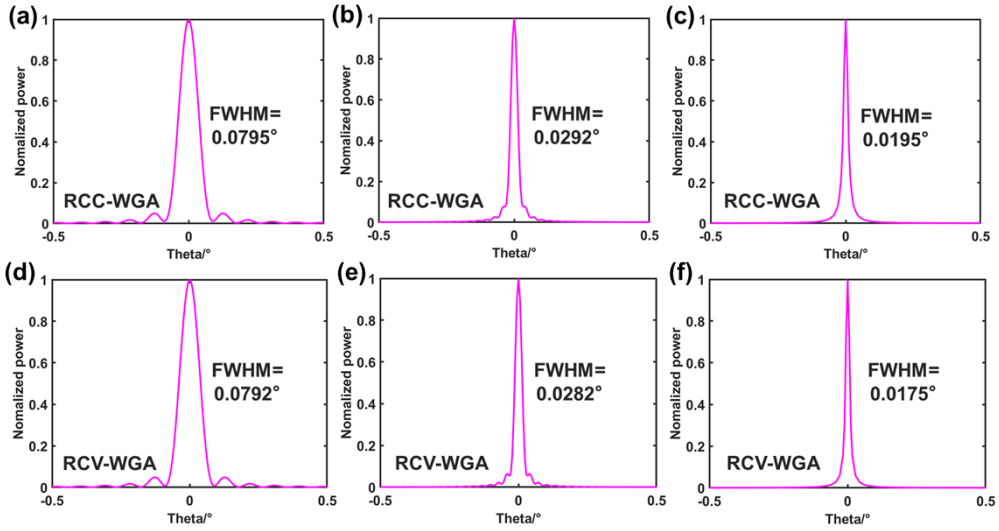

Fig. 7. Calculated beam divergences of two WGAs with various antenna lengths. The lengths of RCC-WGA are (a)1 mm. (b)3 mm. (c)6 mm. With the corresponding beam FWHMs are 0.0795°, 0.0292° and 0.0195° at the wavelength of 1550 nm. The lengths of RCV-WGA are (d)1 mm. (e)3 mm. (f)6 mm. With the corresponding beam FWHMs are 0.0792°, 0.0282° and 0.0175° at the wavelength of 1550 nm.

From Eq. (2)–Eq. (3), we confirm that there are a series of minimum coupling strength κ values with ridge width varying, namely different orders of L-BICs conditions for proposed WGAs. The ridge widths at L-BICs conditions are calculated in Eq. (4)–Eq. (5). It is worth noting that we only introduce lateral destructive interference to suppress lateral scattering fields incompletely as the different amplitudes of two coherent fields, so it is not a perfect BIC condition. The downward diffractive fields can be further decreased by multi-layer grating structures.

$$w_1 = 2w_2 + \frac{\lambda[(2m+1)\pi - \varphi_{0,\lambda}]}{2\pi n_{S,\lambda}} \qquad m = 1, 2, 3 \ldots \tag{4}$$

$$w_1 = \frac{\lambda[(2m+1)\pi - \varphi'_{0,\lambda}]}{2\pi n'_{S,\lambda}} \qquad m = 1, 2, 3 \ldots \tag{5}$$

Optics EXPRESS

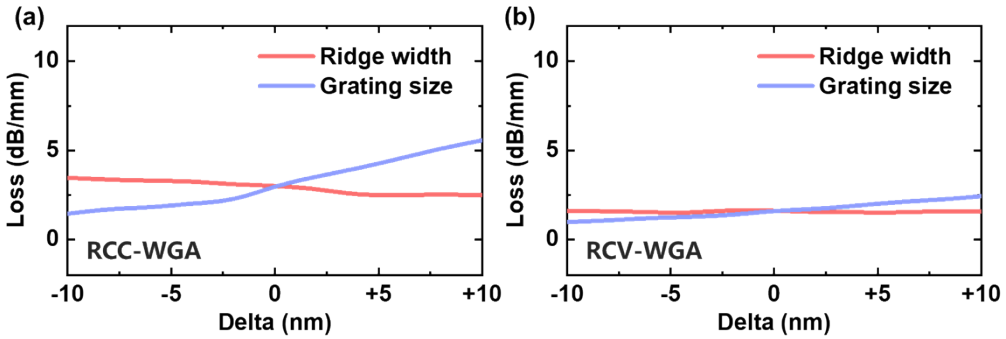

Fig. 8. The loss with fabrication tolerance analysis for the ridge width and teeth size in the range of ±10 nm at the wavelength of 1550 nm. (a) RCC-WGA. (b) RCV-WGA.

We simulate and search the L-BIC conditions upon different ridge widths via three-dimensional finite difference time-domain(3D-FDTD), Fig. 4(b) shows lateral scattering ratio (scattering towards WGA lateral over the total scattering) curves with varied ridge widths at the wavelength of 1550 nm. We define the L-BICs conditions where lateral scattering ratio reach minimum values, as the maximum destructive interference happens. Figure 4(b) indicates that 1-order L-BIC condition of RCC-WGA happens approximately at the ridge width of 0.6μm, while 2-order L-BIC condition happens at 1.2μm. From Fig. 4(a), it's also obviously that the total loss for RCC-WGA also reach minimum values near L-BICs conditions. Although RCC-WGA with higher order L-BIC condition has lower loss and better side scattering ratio, we still choose 1-order L-BIC structure for compact WGA. Similarly, the 1-order and 2-order L-BICs conditions of RCV-WGA happen at the ridge width of 0.5μm and 1.2μm, as shown in Fig. 4(d). For the sake of performance comparison, we set two WGAs to the same ridge width of 0.5μm.

Figure 5 demonstrates the performance of proposed WGAs with the ridge width of 0.5μm. It's distinct that RCC-WGA nearly has a more than half the emitting efficiency in the wide wavelength range of 1480-1580 nm, while RCV-WGA just has an efficiency over 40%. What's more, RCC-WGA has a near zero back reflection ratio, which maintains the input signal undisturbed. RCC-WGA has a more balanced loss level in the wide wavelength range, while RCV-WGA has a lower loss in longer wavelength. Benefit from the L-BIC condition, the WGAs both has a lateral scattering ratio below 40% in the wavelength range of 1480-1580 nm, the directivities of WGAs are more than 60% and 55%. Generally, RCC-WGAs has a relative better performance than RCV-WGA in 100 nm bandwidth. We attribute this to the fact that the inner sides of ridge area have weaker mode field than outer area. By the way, the added power in the mentioned directions may slightly larger than 100%, because the disturbed mode would radiate light around the waveguide section, rather than radiate only in lateral and vertical directions.

As is known to all, the power attenuation principle in WGAs can be expressed as Eq. (6).

$$I_x = I_0 \exp(-\beta_0 x) \tag{6}$$

I_0 is the input power and I_x is the remain light power in WGA at the length position of x, β_0 is the perturbation strength. The perturbation strength β_0 of RCC-WGA and RCV-WGA are calculated as 6.262×10^{-4} μm^{-1} and 4.976×10^{-4} μm^{-1} at the wavelength of 1550 nm, respectively. Here we simulate the two WGAs with 50μm length due to the computational power constraints. The diffraction angles upon wavelength tuning are plotted in Fig. 6. The vertical steering angles of RCC-WGAs are 15.45° and 2.02° at the wavelength of 1480 nm and 1580 nm, while the vertical steering angles of RCV-WGAs are 14.85°, and 1.44°. Therefore, the azimuthal angle steering ranges of two WGAs are 13.43°and 13.41° upon 100 nm wavelength tuning range.

Optics EXPRESS

We calculate the beam divergences with different emitting lengths in theory at the wavelength of 1550 nm. As mentioned in Fig. 6, The near-field attenuations of two WGAs can be expressed as $I_x = I_0\exp[-0.6266x(mm^{-1})]$ and $I_x = I_0\exp[-0.4976x(mm^{-1})]$ at 1550 nm wavelength. We conduct the Fourier transforms to the near-filed with the WGA lengths of 1 mm, 3 mm and 6 mm, hence we get the far-field beam profiles, as shown in Fig. 7. The full width at half maximums (FWHMs) of RCC-WGA are 0.0795°, 0.0292° and 0.0195°. And the beam FWHMs of RCV-WGA are 0.0792°, 0.0282° and 0.0175°. It's consistent with the common sense that a larger emitting aperture owns a narrower beam divergence.

What's more, we also analyze the fabrication tolerance for the proposed WGAs. The fabrication process would lead to size variation, causing the actual device to deviate from our designed parameters. In that case, a more fabrication tolerant WGA is more meaningful in OPAs. We mainly focus on the ridge width in the range of ±10 nm and teeth size in the range of ±10 nm at 1550 nm wavelength, the fabrication error influence is shown in Fig. 8. The fiducial ridge width and teeth size are 500 nm and 70 nm. The RCV-WGA is more error tolerant than RCC-WGA. According to the comprehensive analysis, if the devices size can be fabricated precisely, the RCC-WGA is a better choice.

3. Device fabrication and measurement

As for lithography process, a critical dimension (CD) of 70 nm is unable to fabricate by single lithography process using deep ultraviolet lithography, we utilized electron beam lithography (EBL) and inductively coupled plasma (ICP) etching system to fabricate the WGAs. In the future, it's promising to fabricate the WGAs by utilizing a higher process node lithography.

A commercially available SOI wafer with a 220 nm thick top silicon layer and 2μm buried silicon dioxide is cleaned by sonication in acetone and isopropanol, then dried with N_2 stream. A 360 nm thick ZEP is spin coated on top silicon film as a mask, and metal mark patterns are defined by EBL. The residual coat is cleaned by plasma stripper. After development, a 10 nm/50 nm thick chromium (Cr)/gold (Au) alignment marks is deposited onto the wafer using electron-beam evaporation (EBE), followed by lift-off to reserve metal marks. Then, a 250 nm thick ZEP is spin coated on wafer and the first device patterns are defined by EBL, after development procedure is 70nm-shallow etching by ICP etching system. Next, remove the resist and spin coat a 250 nm thick ZEP again. Subsequently, the second device patterns are also defined by EBL with the same parameters. After development procedure is 220 nm depth etching by ICP etching system. Removing the resist and characterizing device size by scanning electron microscope (SEM). Finally, we clean the wafer, a 2μm thick silicon dioxide film is then deposited on the top surface of the wafer as silica cladding by plasma-enhanced chemical vapor deposition (PECVD). The whole process flow is shown in Fig. 9, a shallow etched ridge waveguide is demonstrated as a gesture. The scanning electron microscope (SEM) images of fabricated RCC-WGA and RCV-WGA are shown in Fig. 10.

A standard vertical fiber-chip coupling system (OMTOOLS OMT-22071401GJ), a tunable narrow-linewidth laser (SANTEC TSL-710) and a power meter are used to measure the transmission spectra of the WGAs. The measured broadband loss curves of two WGAs in the wavelength range of 1480-1580 nm are shown in Fig. 11(a). (c). In order to ensure the superiority of WGAs at L-BIC conditions, we set a pair of WGAs absent from BIC conditions as contrasts, the ridge width is set to 0.3μm and the slab width is 0.6μm. Other parameters are unchanged. The loss curves of control group are shown in Fig. 11(b). (d). The two high-loss peaks due to the form of partly Bragg reflection. It's evident that the WGAs at L-BIC conditions have lower loss and more balanced performance.

The experimental setup for near-field and far-field imaging measurements is a 30 mm coaxial 4f imaging system, an infrared camera is placed to capture emission profiles, as shown in Fig. 12. The 30 mm coaxial 4f imaging system is installed above the fiber-chip coupling system, with

Optics EXPRESS

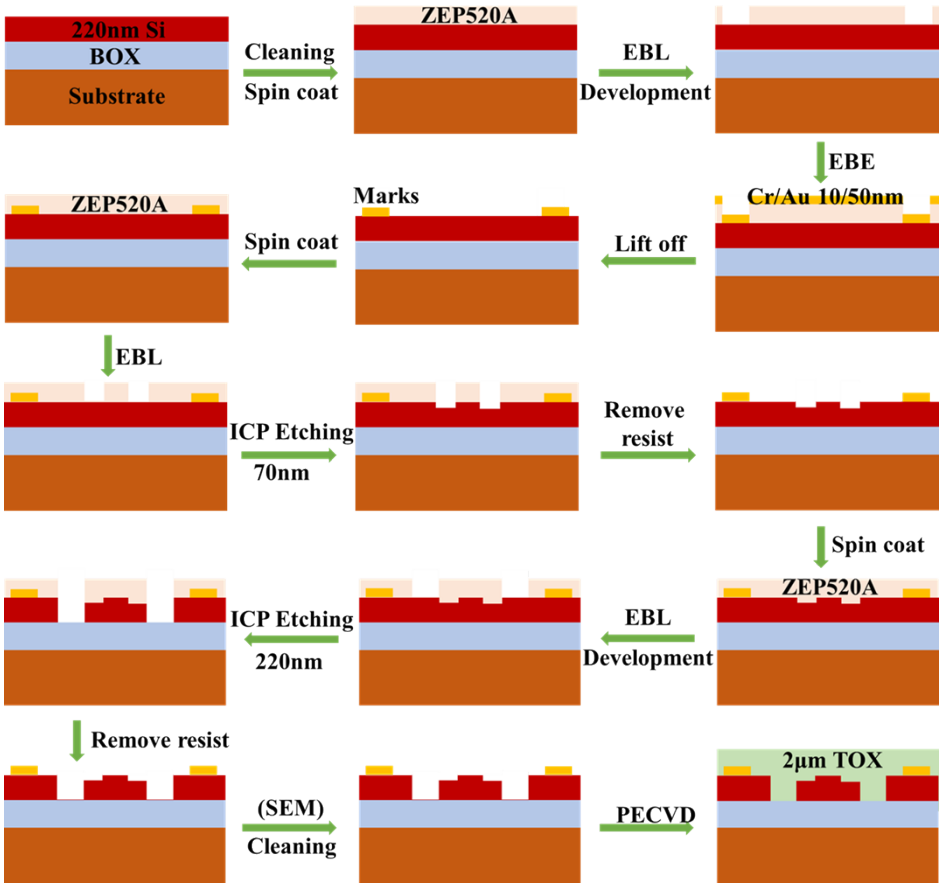

Fig. 9. Procedure for fabricating proposed WGAs.

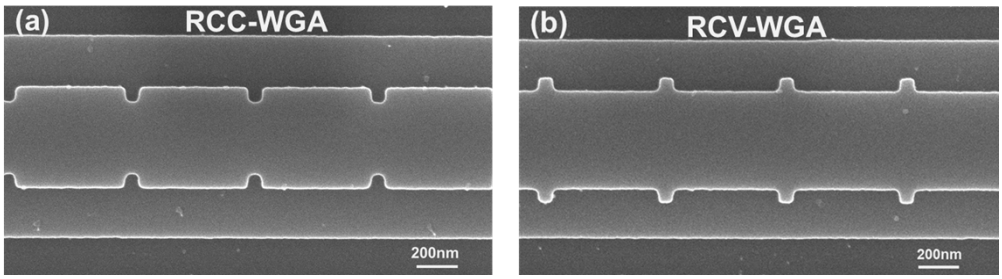

Fig. 10. The scanning electron microscope (SEM) images of fabricated WGAs. (a) RCC-WGA and (b) RCV-WGA.

Optics EXPRESS

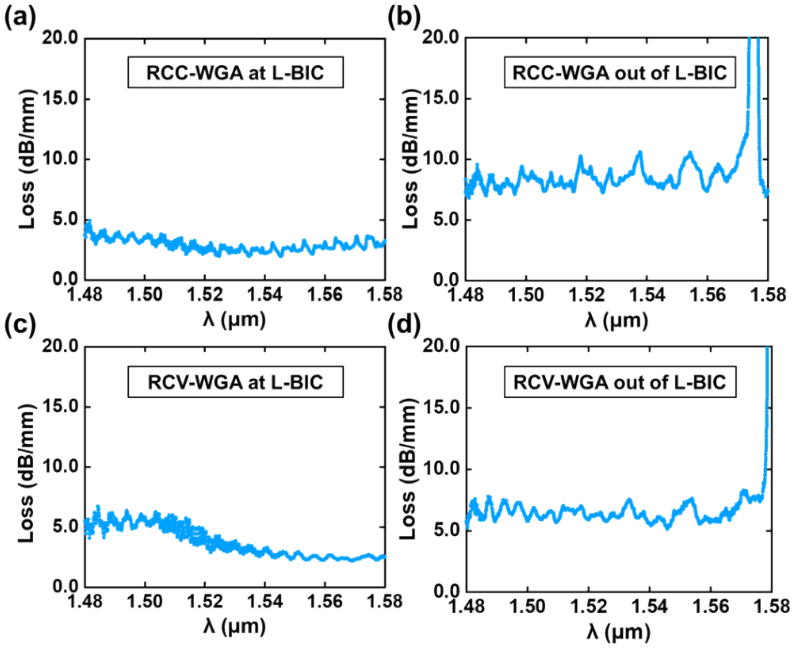

Fig. 11. Measured loss curves of two WGAs at L-BIC condition with the ridge width of 0.5 μm. (a) RCC-WGA. (c) RCV-WGA. Measured loss curves of two WGAs at L-BIC condition with the ridge width of 0.3 μm as a control group. (b) RCC-WGA. (d) RCV-WGA. The advantage at L-BIC conditions is obvious by comparison. The two high loss peaks due to the form of partly Bragg reflection.

two convex lenses. The captured near-field images of RCC-WGA and RCV-WGA are shown in Fig. 13(a). (b). The whole WGAs lengths are both 6 mm. The upper bright spot is input grating coupler area, while the downer bright spot is output grating coupler. The power attenuation process in antennas is clear along the downward direction from the near-field images.

The far-field patterns at 1550 nm wavelength for RCC-WGA and RCV-WGA are plotted in Fig. 14. Unusually, the captured beam shapes consist of a series of light stripes instead of a straight line. To seek the reason of this phenomenon, we adjusted the 4f system to focus from far-field pattern to near-field pattern. We found that the disconnected area is formed as the interference by light from grating couplers or reflected light on the chip surface, as the coupling angle of grating coupler is almost the same with diffractive angle of the WGAs. We mainly choose the undisturbed area and fitted the beam outlines of WGAs, the measured beam FWHMs are 0.0251° and 0.0237° respectively, as shown in Fig. 15.

We use the lenses combination of $f_1 = 7.5$ cm and $f_2 = 6$ cm to measure the steering sensitivities. Limited by the aperture size of the imaging system, we test the steering sensitives by 10 nm wavelength tuning. The far-field patterns of RCC-WGA and RCV-WGA at the wavelength of 1550 nm and 1560 nm are measured in the same field-of-view, as shown in Fig. 16. The working distance of 4f imaging system is 12 cm, the marked moving pixel numbers are 358 and 379, respectively. Thus, the measured steering sensitivities are calculated as 1.28°/10 nm and 1.34°/10 nm.

To have a better comprehension, we supplied a detailed comparison table to show our advantages, as shown in Table 1. The options include platform, layers, length, experimental loss, FWHM, efficiency, directivity, critical dimension (CD) and grating etching depth. By comparing our RCC-WGA with other schemes. It's distinct that our work has a relative sharper IFOV and

Optics EXPRESS

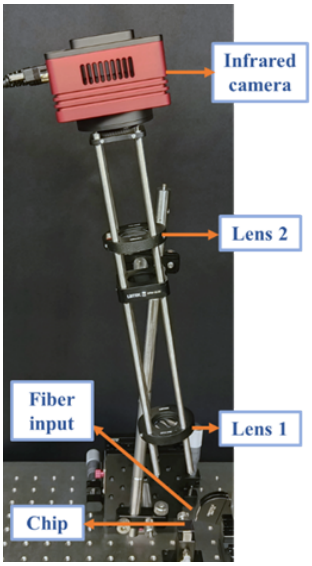

Fig. 12. Schematic of the experimental setup for near-field and far-field imaging measurements.

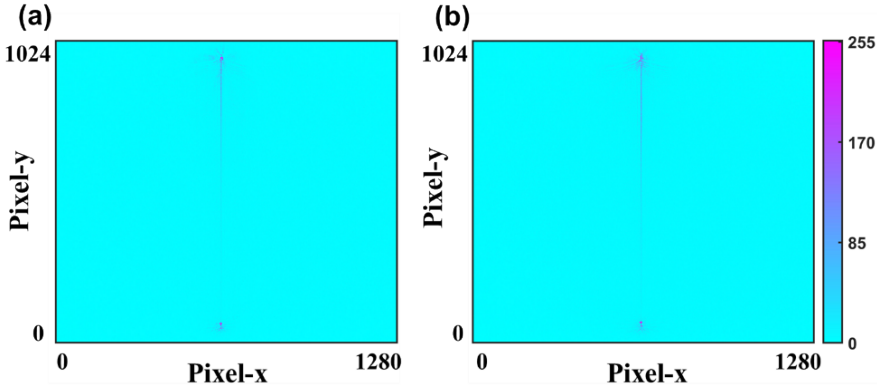

Fig. 13. Measured near-field images for (a) RCC-WGA and (b) RCV-WGA. The upper bright spot is input grating coupler and the under bright spot is output grating coupler. The hole device length is 6 mm, and the power attenuation is indicated.

Optics EXPRESS

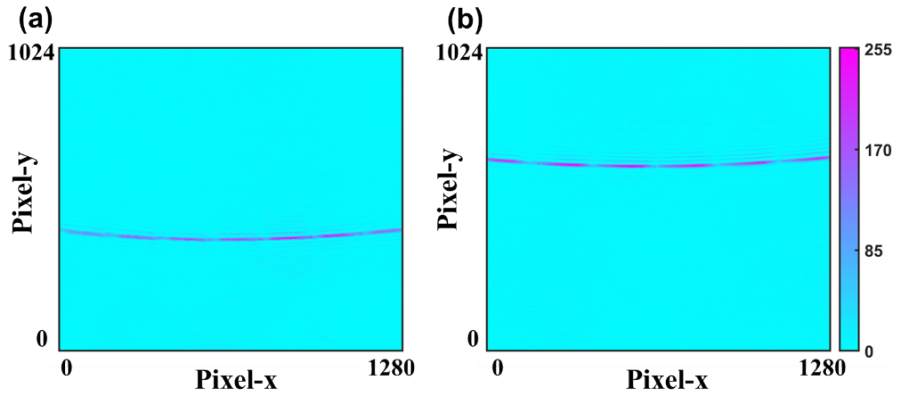

Fig. 14. The far-field images at the wavelength of 1550 nm of (a) RCC-WGA and (b) RCV-WGA.

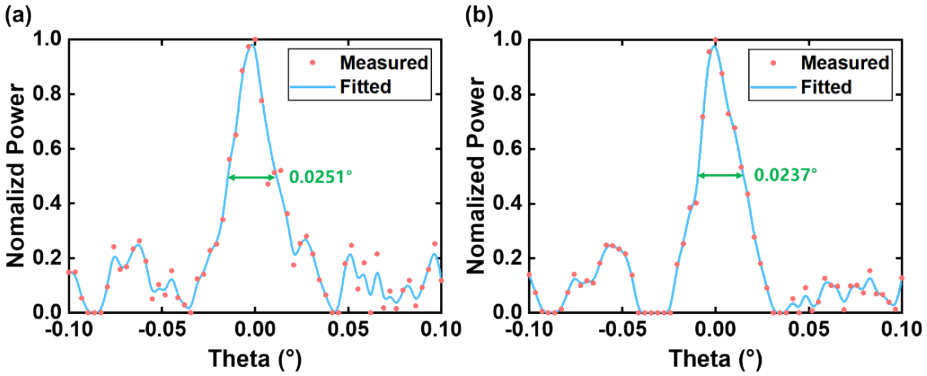

Fig. 15. The measured beam divergences of (a) RCC-WGA and (b) RCV-WGA at the wavelength of 1550 nm. The measured full width at half maximum (FWHM) are 0.0251° and 0.0237°.

larger emitting aperture in comparison to other schemes in SOI platform. The multi-layer antenna is supposed to achieve better directivity and lower loss due to the more degrees of freedom, but brings extra process in fabrication or customized process. What's even rarer, our design is a typical fabrication compatible method. It's easy to fabricate by EBL and ICP etching system. Our method provides a promising method for OPAs in typical SOI platform.

Table 1. Performance comparison for various antennas method

Reference	Platform	layers	Length (/mm)	Loss (dB/mm)	FWHM (°)	Efficiency	Directivity	CD (nm)	Depth (nm)
[17]	SOI	single	4	/	0.08	/	/	280	10
[35]	SOI	single	1	/	0.095	/	/	100	220
[22]	SiN	single	3.16	/	0.04	22.9%	/	75	200
[36]	SiN	double	2.5	/	0.066	/	92%	230	200
[10]	SiN	double	3	/	0.029	/	95%	200	70
[21]	SiN-on SOI	double	2	/	0.1	/	/	86.1	60
[37]	SiN-on SOI	double	1.5	2.27	0.061	/	/	150	400
This work	SOI	single	6	~2.5	0.0251	50%	60%	70	70

Optics EXPRESS

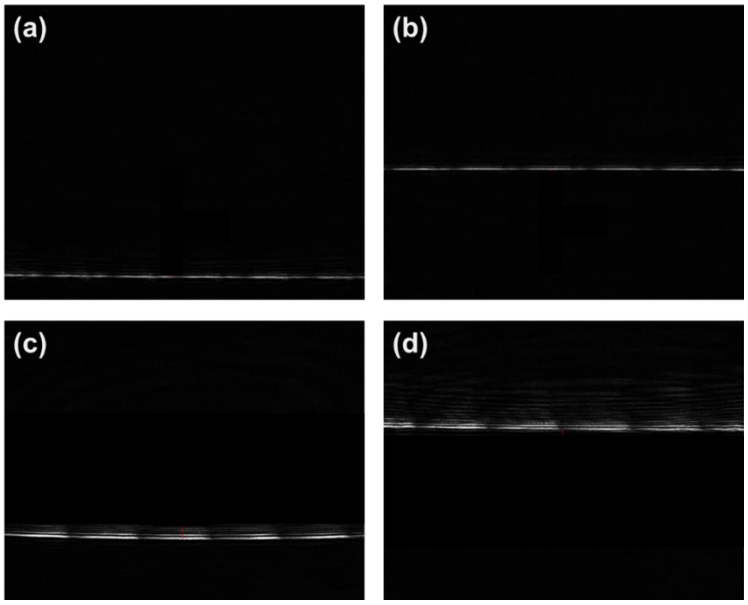

Fig. 16. Measured steering sensitivities in the same field-of-view with a wavelength step of 10 nm. The far-filed patterns of RCC-WGA at the wavelength of (a) 1550 nm. (b) 1560 nm. The far-filed patterns of RCV-WGA at the wavelength of (c) 1550 nm. (d) 1560 nm.

4. Conclusions

In conclusion, we have proposed two ridge-waveguide-based ultralong WGAs with foundry compatible etching process. In the future, it's promising to fabricate the WGAs by utilizing a higher process node lithography. We introduce 1-order L-BIC condition in lateral direction to the WGAs, which restrains the side scattering fields significantly, thereby improves the emitting efficiency and directivity. The minimum antenna loss could be suppressed to even 2 dB/mm and effective antenna length can reach to 6 mm level. RCC-WGA has a relatively better performance than RCV-WGA in the wavelength range of 1480-1580 nm while the RCV-WGA has a better tolerance, we mainly recommended the RCC-WGA. It has a nearly more than 50% emitting efficiency and more than 64% directivity in 100 nm wavelength bandwidth, with almost zero level back reflection. We set up a 30 mm coaxial 4f imaging system to measure near-field and far-field images. The measured beam divergences are 0.0251° and 0.0237°, respectively. We also verify the steering sensitivities of 1.28°/10 nm and 1.34°/10 nm, mainly for the application prospects in OPAs.

Funding. The Key Research and Development Program of Hubei Province (2021BAA004); Innovation Project of Optics Valley Laboratory (OVL2023ZD004); National Natural Science Foundation of China (62105115).

Acknowledgments. The authors thanks engineer Pan Li in the Center of Optoelectronic Micro & Nano Fabrication and Characterizing Facility, Wuhan National Laboratory for Optoelectronics of Huazhong University of Science and Technology for the support in device fabrication.

Disclosures. The authors declare no conflicts of interest.

Data availability. Data underlying the results presented in this paper are not publicly available at this time but may be obtained from the authors upon reasonable request.

References

1. K. Van Acoleyen, W. Bogaerts, J. Jágerská, *et al.*, "Off-chip beam steering with a one-dimensional optical phased array on silicon-on-insulator," Opt. Lett. **34**(9), 1477–1479 (2009).

Optics EXPRESS

2. C. V. Poulton, A. Yaacobi, D. B. Cole, *et al.*, "Coherent solid-state LIDAR with silicon photonic optical phased arrays," Opt. Lett. **42**(20), 4091–4094 (2017).
3. I. Kim, R. J. Martins, J. Jang, *et al.*, "Nanophotonics for light detection and ranging technology," Nat. Nanotechnol. **16**(5), 508–524 (2021).
4. C.-W. Chow, Y.-C. Chang, S.-I. Kuo, *et al.*, "Actively Controllable Beam Steering Optical Wireless Communication (OWC) Using Integrated Optical Phased Array (OPA)," J. Lightwave Technol. **41**(4), 1122–1128 (2023).
5. Q. You, D. Chen, X. Xiao, *et al.*, "10 Gb/s free space optical interconnect with broadcasting capability enabled by a silicon integrated optical phased array," Chin. Opt. Lett. **19**(12), 120602 (2021).
6. Y. Kohno, K. Komatsu, R. Tang, *et al.*, "Ghost imaging using a large-scale silicon photonic phased array chip," Opt. Express **27**(3), 3817–3823 (2019).
7. C. V. Poulton, M. J. Byrd, M. Raval, *et al.*, "Large-scale silicon nitride nanophotonic phased arrays at infrared and visible wavelengths," Opt. Lett. **42**(1), 21–24 (2017).
8. N. A. Tyler, D. Fowler, S. Malhouitre, *et al.*, "SiN integrated optical phased arrays for two-dimensional beam steering at a single near-infrared wavelength," Opt. Express **27**(4), 5851–5858 (2019).
9. P. Wang, G. Luo, Y. Xu, *et al.*, "Design and fabrication of a SiN-Si dual-layer optical phased array chip," Photonics Res. **8**(6), 912–919 (2020).
10. Y. Li, B. Chen, Q. Na, *et al.*, "Wide-steering-angle high-resolution optical phased array," Photonics Res. **9**(12), 2511–2518 (2021).
11. G. Yue and Y. Li, "Integrated lithium niobate optical phased array for two-dimensional beam steering," Opt. Lett. **48**(14), 3633–3636 (2023).
12. M. Gagino, M. B. J. v. Rijn, E. A. J. M. Bente, *et al.*, "Broadband Operation of an InP Optical Phased Array," IEEE Photonics Technol. Lett. **34**(10), 541–544 (2022).
13. S. Tan, X. Dai, J. Lou, *et al.*, "Low-power consumption InP-based optical phase arrays with non-uniformly spaced output waveguides," Opt. Express **31**(2), 3199–3211 (2023).
14. J. C. Hulme, J. K. Doylend, M. J. R. Heck, *et al.*, "Fully integrated hybrid silicon two dimensional beam scanner," Opt. Express **23**(5), 5861–5874 (2015).
15. W. Xu, Y. Guo, X. Li, *et al.*, "Fully Integrated Solid-State LiDAR Transmitter on a Multi-Layer Silicon-Nitride-on-Silicon Photonic Platform," J. Lightwave Technol. **41**(3), 832–840 (2023).
16. Y. Zhang, Y.-C. Ling, K. Zhang, *et al.*, "Sub-wavelength-pitch silicon-photonic optical phased array for large field-of-regard coherent optical beam steering," Opt. Express **27**(3), 1929–1940 (2019).
17. Y. Liu and H. Hu, "Silicon optical phased array with a 180-degree field of view for 2D optical beam steering," Optica **9**(8), 903–907 (2022).
18. J. Chen, J. Wang, J. Li, *et al.*, "Subwavelength structure enabled ultra-long waveguide grating antenna," Opt. Express **29**(10), 15133–15144 (2021).
19. P. Ginel-Moreno, A. Sánchez-Postigo, J. de-Oliva-Rubio, *et al.*, "Millimeter-long metamaterial surface-emitting antenna in the silicon photonics platform," Opt. Lett. **46**(15), 3733–3736 (2021).
20. M. Raval, C. V. Poulton, and M. R. Watts, "Unidirectional waveguide grating antennas with uniform emission for optical phased arrays," Opt. Lett. **42**(13), 2563–2566 (2017).
21. K. Shang, C. Qin, Y. Zhang, *et al.*, "Uniform emission, constant wavevector silicon grating surface emitter for beam steering with ultra-sharp instantaneous field-of-view," Opt. Express **25**(17), 19655–19661 (2017).
22. L. Yu, P. Ma, G. Luo, *et al.*, "Adoption of large aperture chirped grating antennas in optical phase array for long distance ranging," Opt. Express **30**(15), 28112–28120 (2022).
23. H. Qiu, Y. Liu, X. Meng, *et al.*, "Bidirectional high sidelobe suppression silicon optical phased array," Photonics Res. **11**(4), 659–668 (2023).
24. C. W. Hsu, B. Zhen, A. D. Stone, *et al.*, "Bound states in the continuum," Nat. Rev. Mater. **1**(9), 16048 (2016).
25. C. Zou, J. Cui, F. Sun, *et al.*, "Guiding light through optical bound states in the continuum for ultrahigh-Q microresonators," Laser Photonics Rev. **9**(1), 114–119 (2015).
26. E. A. Bezus, D. A. Bykov, and L. L. Doskolovich, "Bound states in the continuum and high-Q resonances supported by a dielectric ridge on a slab waveguide," Photonics Res. **6**(11), 1084–1093 (2018).
27. P. Wang, F. He, J. Liu, *et al.*, "Ultra-high-Q resonances in terahertz all-silicon metasurfaces based on bound states in the continuum," Photonics Res. **10**(12), 2743–2750 (2022).
28. Z. Yu, X. Xi, J. Ma, *et al.*, "Photonic integrated circuits with bound states in the continuum," Optica **6**(10), 1342–1348 (2019).
29. Z. Yu, Y. Tong, H. K. Tsang, *et al.*, "High-dimensional communication on etchless lithium niobate platform with photonic bound states in the continuum," Nat. Commun. **11**(1), 2602 (2020).
30. X. Li, J. Ma, S. Liu, *et al.*, "Efficient second harmonic generation by harnessing bound states in the continuum in semi-nonlinear etchless lithium niobate waveguides," Light-Sci. Appl. **11**(1), 317 (2022).
31. F. Ye, Y. Yu, X. Xi, *et al.*, "Second-Harmonic Generation in Etchless Lithium Niobate Nanophotonic Waveguides with Bound States in the Continuum," Laser Photonics Rev. **16**(3), 2100429 (2022).
32. H. Xu and Y. Shi, "Diffraction engineering for silicon waveguide grating antenna by harnessing bound state in the continuum," Nanophotonics **9**(6), 1439–1446 (2020).
33. H. Xu and Y. Shi, "Silicon-Waveguide-Integrated High-Quality Metagrating Supporting Bound State in the Continuum," Laser Photonics Rev. **14**(6), 1900430 (2020).

Optics EXPRESS

34. Z. Ma, Y. Fu, Y. Wan, *et al.*, "Bound State in the Continuum Enabled Ultralong Silicon Waveguide Grating Antennas for Integrated LiDAR Applications," *2023 Asia Communications and Photonics Conference/2023 International Photonics and Optoelectronics Meetings (ACP/POEM)*, 2023, 1–3.
35. W. Yao, Z. Huang, J. Chen, *et al.*, "Ultralong waveguide grating antenna enabled by evanescent field modulation," Opt. Lett. **47**(20), 5397–5400 (2022).
36. Z. Wang, L. Yu, Y. Yang, *et al.*, "Wide field of view optical phased array with a high-directionality antenna," Opt. Express **31**(13), 21192–21199 (2023).
37. J. Duan, W. Yao, X. Zhao, *et al.*, "Vertical directional coupling based grating emission engineering for optical phased arrays," Opt. Lett. **49**(11), 3102–3105 (2024).